Editors' Suggestion

Effect of polymer injection on the development of a trip-wire-induced bypass transitioning boundary layer

Yash Shah and Serhiy Yarusevych*
Mechanical and Mechatronics Engineering, University of Waterloo, Waterloo N2L 3G1, Canada

(Received 23 September 2021; accepted 8 August 2022; published 8 September 2022)

An experimental investigation is conducted to evaluate the effect of polymer injection on the development of a zero-pressure-gradient bypass transitioning boundary layer on a flat plate. Planar particle image velocimetry and planar laser-induced fluorescence measurements conducted at multiple streamwise stations allow for a characterization of the development of the bypass transition process induced by a two-dimensional trip wire in both Newtonian and polymer-injected flow. Two different trip placements with respect to the injection slot are considered to study the effect of polymer injection within the wake of the trip wire and within the laminar boundary layer upstream of the trip. The transition process is initiated in a separated shear layer downstream of the trip wire, where a rapid amplification of the velocity perturbations via an inflectional Kelvin-Helmholtz instability leads to vortex shedding and subsequent breakdown to turbulence. A similar transition process is observed with polymer injection, but a more rapid initial growth of perturbations is observed, leading to earlier transition. Nonetheless, an onset of polymer effect is seen in the late transition stages and leads to significant levels of drag reduction in the developing turbulent boundary layer.

DOI: 10.1103/PhysRevFluids.7.093901

I. INTRODUCTION

The phenomenon of drag reduction caused by the introduction of polymer additives in turbulent boundary layers has been widely studied for a number of engineering applications including, but not limited to, oil recovery and transport, marine vehicles, sewers, and irrigation [1–6]. Most of these applications being primarily in the regime of turbulent flow, the topic of turbulence control with polymer injection has seen a tremendous research activity to examine the polymer's ability to suppress turbulence within the boundary layer resulting in decrease in skin friction [7–10]. Recent studies have exploited both advanced measurement techniques like particle image velocimetry (PIV) [11–15] and computational simulations [16–19] to highlight the interactions of polymer and turbulent motions. In contrast, very few studies have considered the effect of polymer additives on the laminar-to-turbulent transition, where potential benefits could be derived by suppressing turbulent motions and thereby delaying transition.

The *natural* process of laminar-to-turbulent transition occurs in a boundary layer with low levels of external disturbances (Tu $< 0.1\%$, where Tu is the turbulence intensity) wherein the disturbances enter the boundary layer and amplify in the near-wall region through the well known Tollmien-Schlichting waves before the ensuing nonlinear interactions lead to turbulent breakdown [20]. The initial stage of this process is well described by the linear stability theory [21–23] and has been documented in various scenarios through experimental studies [20,24–26]. The transition process is said to be *bypassed* when the initial amplification of disturbances is rapid and leads to a much

*syarus@uwaterloo.ca

earlier transition to turbulence [20,27]. This form of transition is not as well understood and occurs in the presence of relatively high levels of external disturbances (Tu > 0.5%) [28–30] and/or surface roughness among a number of other factors [31–34]. The bypass transition process is of practical significance for a number of engineering applications including flows over marine vehicles due to bio-fouling of the external surfaces [35,36]. Thus, the effect of polymer injection in the transitioning flow region and the ensuing turbulent boundary layer development is of particular interest.

The bypass transition in the flat-plate boundary layer is characterized by low frequency oscillations in the streamwise velocity leading to the formation of low- and high-speed streaks [29,37–39]. These streaky structures are also known to undergo various modes of instabilities and oscillate in the spanwise direction with the peak-to-peak amplitudes on the order of the freestream velocity [40,41]. The eventual intermittent appearance of turbulence spots has been attributed to the breakdown of the streaky structure due to secondary instabilities, adding to the complexity of the transition mechanism [29,42–46]. Pioneering studies by Emmons [47] and Dhawan and Narasimha [48] illustrate the universality of the intermittency in the late transition stages in both classical and bypass transitioning boundary layers produced by various means, highlighting the similarity and dominance of the turbulence spots within these stages. More recent investigations provide a detailed account of the associated flow dynamics in the vicinity of such turbulent events [29,42,49].

The effect of polymer injection on laminar-to-turbulent transition has been explored in pipe flows [50–55] where the later stages of transition involve intermittent formation of turbulent puffs and slugs following the amplification of the local perturbations [56–58]. These investigations produced inconsistent results, potentially due to significant differences in experimental setups. In most investigations, no distinct effect of polymers on the transition process was observed. Draad *et al.* [50] noted that this can be potentially attributed to common experimental setup issues, namely, high inlet disturbances from the pumps and the use of relatively large-diameter pipes in which the onset shear stress [59] for the polymers could not be achieved within the laminar regime. Coiled polymer conformations, low molecular weights [$O(10^5)$], and polymer degradation due to metallic meshes used to condition the pipe flow in the above studies have also been attributed to cause an increase in the onset shear stress, which may have prevented polymer action and led to a premature transition [50]. However, a distinct delay in transition has been observed in a few studies where the above factors were carefully controlled in addition to employing higher molecular weight polymers [$O(10^6)$] and helical conformations with both low and high concentration solutions [60–62].

Recent viscoelastic numerical simulations in channel flows have also investigated the mechanisms of polymer drag reduction at transitional Reynolds numbers ($\mathrm{Re}_\tau = 70$–130) [63–65]. These studies have shown that the near-wall flow dynamics resulting from intermittent regions of high and low turbulence activity are significantly modified by the introduction of viscoelasticity. While such localized regions of low turbulence, or *hibernating* regions, are also found in Newtonian channel flows [66–68], they are shown to expand with increasing Weissenberg number ($\mathrm{Wi} = t_{\mathrm{rel}}\dot{\gamma}$, where t_{rel} is the polymer relaxation time and $\dot{\gamma}$ is the characteristic shear rate of the flow), leading to drag reduction within the transitional regime. Similar expansions of the hibernating regions were noted within the buffer layer of polymer injected fully developed turbulent boundary layers [13,69].

Despite an enhanced understanding of the mechanisms of polymer drag reduction in turbulent boundary layers and exploratory studies on polymer effect on transition in channel flows, to the best of the authors' knowledge, the polymer effect on laminar-to-turbulent transition in boundary layers has yet to be investigated. Thus, the present work studies the effect of slot-injected polymer solutions in bypass transitioning flat-plate boundary layers with the goal to examine the development of salient flow features via two-dimensional PIV and planar-laser-induced-fluorescence (PLIF) measurements. The measurements are conducted at multiple stations within an extended length of the transitional flat-plate boundary layer which is produced by a two-dimensional spanwise trip wire. Furthermore, two different injection slot locations with respect to the trip wire are considered providing important insights for the practical implementation of this flow control approach as well as a holistic understanding of the polymer effect on the transitioning flow.

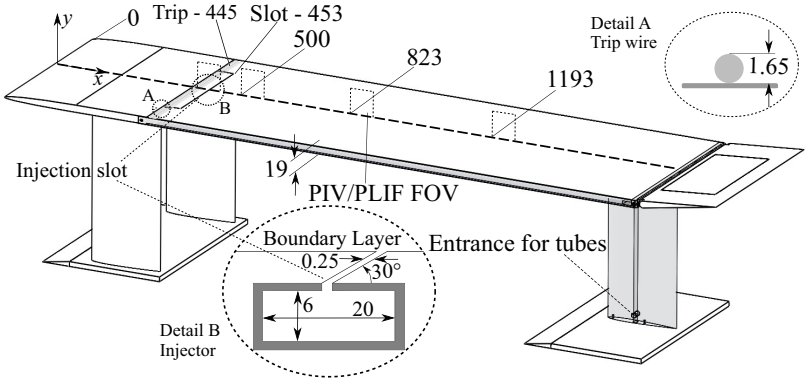

FIG. 1. Schematic of the flat-plate model showing the coordinate system, polymer injection setup, and details of the trip wire. All dimensions are in mm but are not to scale. For clarity, only four PIV measurement stations are shown here corresponding to the trip-upstream case.

II. EXPERIMENTAL METHODOLOGY

A. Facility, model, and polymer injection

The experiments were conducted in a constant-head, closed-loop water tunnel facility at the University of Waterloo with the boundary layer measurement surface being a flat-plate model shown in Fig. 1. The tunnel has a test section length of 2.5 m and a cross section of 0.8×0.5 m^2. The facility is capable of achieving flow velocities of up to 0.5 ms^{-1} with both flow uniformity and freestream turbulence intensity being within 1%. The flat-plate model has a length (L) of 2200 mm and a surface roughness of 0.5 μm. A 0.25 mm-wide spanwise slot is present on the flat plate at $x/L \approx 0.21$ to provide a uniform tangential injection into the boundary layer. A detailed description of the flat-plate model and the facility is provided in Shah and Yarusevych [12]. The tunnel was operated at a freestream velocity of 0.3 ms^{-1} for the cases studied in the present work, resulting in a laminar boundary layer thickness of $\delta_{\text{slot}} = 5.80$ mm at the injection slot.

Bypass transition over an extended length on the flat plate was achieved using a two-dimensional spanwise round trip wire with a diameter of 1.65 mm. Two different configurations were considered based on the trip location relative to the slot, with the trip wire placed 8 mm upstream and 15 mm downstream of the injection slot, which correspond to local laminar boundary layer thicknesses of 5.50 mm and 6.05 mm, respectively. These configurations are denoted as the trip-upstream and the trip-downstream configurations in the present study. The use and sizing of a two-dimensional trip follows a well-established practice from prior experiments (e.g., [70–72]). For a given trip geometry, its efficiency depends on the Reynolds number based on the height (k) of the roughness element ($\text{Re}_k = kU_k/\nu$, where U_k is the streamwise velocity in the laminar boundary layer at the height k from the wall) [73]. For the two configurations investigated in the present study, the trip locations and the wire diameter were chosen such that Re_k, estimated to be 229 and 210, at the upstream and downstream trip locations respectively, falls in the range of the critical Reynolds numbers required to produce a transitional flow [72]. Based on preliminary experiments, for $\text{Re}_k < 180$, the flow did not fully transition over the length of the flat plate, while for $\text{Re}_k > 300$, a rapid transition effectively localized at the trip wire is expected [72].

TABLE I. Test matrix. Coordinate ranges corresponding to the streamwise extent of the field of view and the boundary layer parameters measured for the baseline case at the center of each FOV are provided. † indicates water injection. ‡ indicates that PLIF measurements were performed at two locations $x - x_{\text{inj}} = [-1, 39]$ and $[15, 55]$. $\lambda_0 = \nu/u_{\tau_0}$, where u_{τ_0} is the friction velocity.

Experimental parameters							
Trip-upstream ($x_{\text{trip}} - x_{\text{inj}} = -8$ mm, $U_\infty = 0.3\,\text{ms}^{-1}$, $c_{\text{inj}} = 0^\dagger$, 1000 ppm)							
x/L	$x - x_{\text{inj}}$ (mm)	$x - x_{\text{trip}}$ (mm)	δ_0 (mm)	λ_0 (μm)	Re_{τ_0}	Re_{δ^*}	PLIF (yes/no)
[0.201, 0.220]	[−10, 30]	[−2, 38]	6.13	—	—	923	Yes
[0.227, 0.245]	[47, 87]	[55, 95]	6.99	139.8	50	734	Yes
[0.238, 0.256]	[70, 110]	[78, 118]	7.30	102.8	71	634	Yes
[0.265, 0.283]	[130, 170]	[138, 178]	8.00	69.5	115	555	Yes
[0.292, 0.310]	[190, 230]	[198, 238]	11.05	60.7	182	504	Yes
[0.329, 0.347]	[270, 310]	[278, 318]	12.24	63.4	193	553	Yes
[0.374, 0.392]	[370, 410]	[378, 418]	14.74	65.2	226	679	No
[0.420, 0.438]	[470, 510]	[478, 518]	16.77	66.3	253	770	Yes
[0.465, 0.483]	[570, 610]	[578, 618]	17.98	68.6	262	812	No
[0.542, 0.560]	[740, 780]	[748, 788]	21.53	68.6	314	997	No
Trip-downstream ($x_{\text{trip}} - x_{\text{inj}} = 15$ mm, $U_\infty = 0.3\,\text{ms}^{-1}$, $c_{\text{inj}} = 0^\dagger$, 1000 ppm)							
[0.204, 0.222]	[−5, 35]	[−20, 20]	6.14	—	—	872	Yes‡
[0.240, 0.258]	[75, 115]	[60, 100]	7.45	149.0	50	762	Yes
[0.265, 0.283]	[130, 170]	[115, 155]	7.70	113.2	68	725	Yes
[0.292, 0.310]	[190, 230]	[175, 215]	7.90	77.5	102	661	Yes
[0.338, 0.360]	[290, 330]	[275, 315]	10.08	62.2	162	551	Yes
[0.429, 0.447]	[490, 530]	[475, 515]	14.62	62.7	233	668	Yes
[0.542, 0.560]	[740, 780]	[725, 765]	19.58	65.7	298	913	No
Laminar-No trip ($U_\infty = 0.3\,\text{ms}^{-1}$, $c_{\text{inj}} = 0^\dagger$, 1000 ppm)							
[0.201, 0.220]	[−10, 30]	—	5.91	111.7	53	581	No
[0.292, 0.310]	[190, 230]	—	7.62	120.3	63	724	No
[0.383, 0.401]	[390, 430]	—	8.83	129.5	68	828	No
[0.451, 0.470]	[540, 580]	—	10.03	134.5	75	921	No
[0.542, 0.560]	[740, 780]	—	10.89	134.0	81	981	No

The polymer used in this study was polyethylene oxide (Sigma Aldrich, Inc.) with an average molecular weight of 8×10^6 g/mol. Polymer solutions with a concentration of 1000 ppm were prepared using the protocol developed by [12], which have been verified experimentally to produce consistent results. The employed polymer concentration exceeds the overlap concentration for this polymer ($c^* = 330$ ppm, using Mark-Houwink relationship [74]), and thus, the injected polymer solutions are expected to be in a semidilute state. Seeding particles used for PIV measurements were stirred with the polymer solutions in order to achieve uniform seeding density in the particle images. The injection on the measurement surface was performed by pumping the polymer solutions via a peristaltic pump (AOBL BT101S) with a normalized injection rate of $Q_{\text{inj}}/Q_s = 0.086$ (Q_{inj} is the injection flow rate and $Q_s = 67.3\nu$ is the discharge in the viscous sublayer of a turbulent boundary layer ($y^+ < 11.6$) per unit width [75]) and mean injection velocity of $u_{\text{inj}} = 0.025\,\text{ms}^{-1}$. These injection parameters were shown to produce negligible effects of benign injection in a turbulent boundary layer by previous studies using the same setup [12,13] and did not produce a significant effect on bypass-transition process in the present investigation.

B. Planar PIV and PLIF measurements

Planar PIV measurements were conducted in the x-y plane at multiple streamwise stations at the midspan of the plate (Table I). Prior to the measurements of the two bypass transition cases

with the trip wire, PIV measurements were performed in the laminar boundary layer to establish the baseline boundary layer development on the flat plate. In each of the three cases, injection of water and polymer with $c_{\text{inj}} = 1000$ ppm were included along with the baseline Newtonian flow. Measurements were performed for several fields of view positioned along the plate.

The PIV measurements were conducted using an Imager sCMOS CLHS camera with a sensor size of 2560 × 2160 pixel, a pixel pitch of 6.5 μm, and a digital resolution of 16 bits. The camera was equipped with a 200 mm fixed focal length Nikkor macro lens set to an aperture of $f_{\#} = 5.6$. In order to minimize the ambient noise in the images, a green band-pass filter was mounted in front of the lens. The camera imaged a field of view (FOV) of $38.4 \times 32.4\,\text{mm}^2$ with a resolution of $66.7\,\text{pixelm}^{-1}$m. The illumination of the FOV was provided with a 527 nm Nd:YLF Laser (Photonics Industries DM20), which was synchronized with the camera by a programmable timing unit (PTUx) and controlled via DaVis 10.0 software (LaVision GmbH). The camera and the laser sheet were positioned by two remotely controlled traversing systems which had a resolution of 5 μm. The flow was seeded with hollow glass spheres (Potters, Inc.) with a mean particle diameter of 10 μm and a specific gravity of 1.1 g/cc. For each experimental condition, 4500 double-frame image pairs were acquired with a time separation $\Delta t = 1000\,\mu\text{s}$ and an acquisition frequency of 15 Hz. This corresponded to a mean particle displacement of approximately 20 pixels in the freestream. The uncertainty due to random errors in instantaneous vector fields was estimated to be less than 0.5% of U_∞ with 95% confidence limits.

The signal-to-noise ratio of the particle images was improved by preprocessing the images using a minimum intensity subtraction time-series filter with a kernel of 15 images, and normalization by the ensemble average to mitigate reflections at the wall and spatial variations in the light intensity. The preprocessed images were processed using the ensemble-of-correlation algorithm [76,77] to produce a time-averaged velocity vector field with a final window size of 4 × 4 pixels and an overlap of 50%. The mean vector fields resulting from this procedure have a vector pitch of 30 μm and were used as an initial displacement predictor for a sequential-correlation algorithm used to obtain instantaneous velocity fields. The employed iterative correlation with window deformation had a final window size of 24 × 24 and 75% overlap resulting in a vector pitch of 90 μm.

For the bypass transition cases, PLIF measurements were conducted with both water and polymer injection at selected streamwise stations indicated in Table I. The injected solutions were doped with Rhodamine-6G fluorescent dye following the procedure of Motozawa *et al.* [78], and a similar technique was employed by several previous studies in polymer injected fully developed turbulent boundary layers (e.g., [79,80]). Imaging was performed using the same laser and camera setup as that used for PIV, except that a yellow band-pass filter was used to capture the fluorescent emission of the dye. In this case, 2000 images were acquired in the single frame mode at an acquisition frequency of 50 Hz for each experimental condition. Time-averaged local concentrations, which are based on the temporal average of all the samples within a given single data set, relative to a reference concentration (c_{ref}) at each measurement station were estimated based on the expected linear relationship between the light intensity and the concentration of the weakly excited dye [78,81].

C. Estimation of wall-shear stress

In order to elucidate the associated changes in the skin friction coefficient ($C_f = \tau_w/(0.5\rho U_\infty^2)$), an accurate estimation of the wall-shear stress (τ_w) is essential. In the present study, the wall-shear stress ($\tau_w = \mu d\langle u\rangle/dy|_w$) is estimated based on the estimation of the wall-normal gradient of the mean streamwise velocity ($d\langle u\rangle/dy|_w$). The latter is computed from ensemble-of-correlation results based on 10 to 16 velocity vectors in the near-wall region where the near-wall law $u^+ = y^+$ is expected to be applicable, i.e., within $y^+ \leqslant 5$ [82]. Profiles of streamwise velocity at a representative location in Figs. 2(a) and 2(b) illustrate this linearity in the near-wall data in both Newtonian and polymer injected cases. Note that only every third data point is shown in Fig. 2(b). With the obtained wall-normal velocity gradient, the wall-shear stress, and the skin friction coefficient are estimated

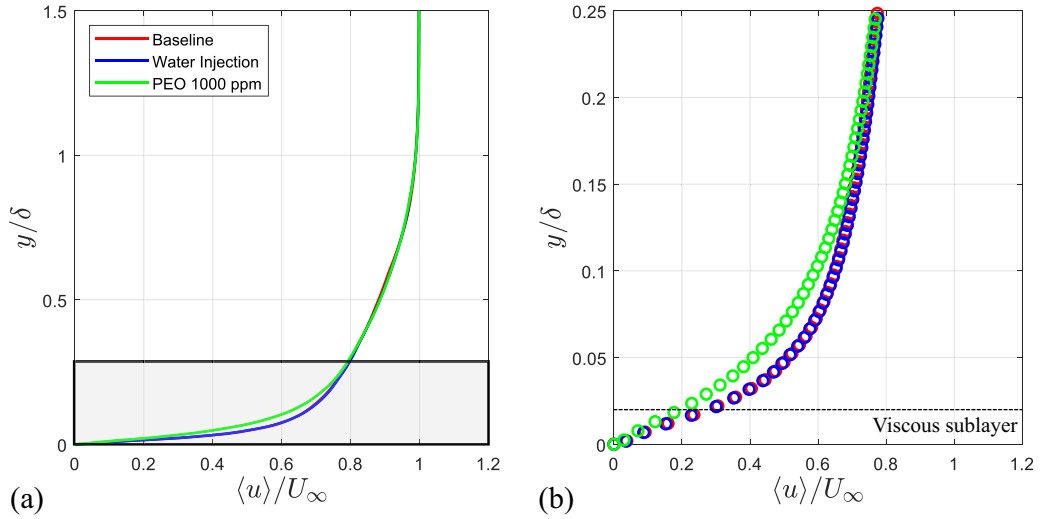

FIG. 2. (a) Time-averaged profiles of streamwise velocity at a representative location and (b) zoomed-in view of the profiles close to the wall as indicated by the black rectangle in (a). For clarity, every third data point is plotted in (b). Dashed line shows the edge of the viscous sublayer considered at $y^+ = 5$ for the baseline flow.

using the fluid properties of water at the measured freestream temperature. Further, to reduce measurement errors, a sliding average operation on the local estimates of C_f is performed over a window of 2 mm in the x direction (equivalent to 68 velocity vectors), similar to the procedure used in turbulent boundary layers by previous studies employing optical techniques [12,83]. It should be noted that the estimates of C_f in the polymer-injected cases are obtained by utilizing the fluid properties of the base medium (water) due to the lack of measurements for the local viscosity of the polymer. This procedure is expected to produce reliable estimates of C_f in the later stages of transition and the turbulent regimes where sufficient mixing of polymer with the base media has occurred leading to the maximum concentrations to be within the limits of overlap concentration for the employed polymer.

III. RESULTS AND DISCUSSION

A. Transitional flow visualization and concentration diffusion

The development of the transitioning boundary layer induced by the trip wire is first studied using flow visualization and concentration of the injected dye obtained from the PLIF measurements. Representative instantaneous flow visualization images for both the trip position upstream and downstream of the injection slot are presented in Figs. 3(a) and 3(b), respectively, with the cases corresponding to water (passive tracer) and polymer injection shown in rows marked (i) and (ii), respectively, for each trip position. The initial development of the tripped boundary layer flow in both cases show that the injected fluid is concentrated in a separated shear layer forming due to flow separation from the trip. The separated shear layer is highly unstable and the attendant Kelvin-Helmholtz (K-H) instability rapidly manifests in the growth of perturbations and roll-up visualized by the entrained dye. The distinct evidence of the periodically shed vortices can be seen within $10 < (x - x_{\text{trip}})/\delta_{\text{slot}} < 16$ in all the cases considered. Consecutively shed corotating vortices undergo merging downstream, resulting in doubling of the primary wavelength, as indicated in Figs. 3(a)(i) and 3(b)(i), consistent with the vortex merging in free shear layers (e.g., Ho and Huerre [84]) and near-wall separating-reattaching flows (e.g., Kurelek *et al.* [85]). An instantaneous snapshot of the vortex merging is seen at $(x - x_{\text{trip}})/\delta_{\text{slot}} \approx 14$ in Fig. 3(b)(i). Moreover, an

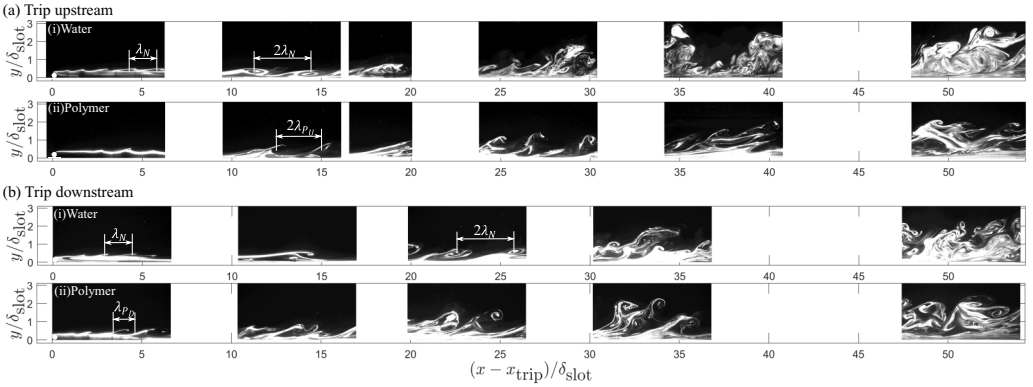

FIG. 3. Instantaneous flow visualization of the injected fluid in (a) trip upstream and (b) trip downstream case. (a)(i) and (b)(i) show injected flow development with water injection (passive tracer), whereas (a)(ii) and (b)(ii) show the development with polymer injection for each of the transition cases, respectively. The coordinate axes are normalized by the laminar boundary layer thickness measured at the injection slot (δ_{slot}). The injection slot is located at $(x - x_{trip})/\delta_{slot} \approx 1.38$ in (a)(i) and (a)(ii), whereas it is located at $(x - x_{trip})/\delta_{slot} \approx -2.6$ in (b)(i) and (b)(ii) and, thus, not shown.

occasional merging of multiple consecutive vortices is also observed within this streamwise range in all the cases. As these spanwise-oriented vortical structures convect downstream, they are seen to lift up and eventually break down due to secondary three-dimensional instabilities that lead to the formation of Λ vortices, transitional-turbulent spots, and hairpin-like vortices [71,86].

Despite the similarities in the transition process, the flow visualizations for the polymer-injected flow cases considered in Figs. 3(a)(ii) and 3(b)(ii) show notable differences close to the trip wire in comparison to the Newtonian flow. While the transition process initiates with formation of the K-H instabilities, the primary streamwise wavelength associated with vortex shedding is observed to decrease from $\lambda_N \approx 1.5\delta_{slot}$ in the baseline flow to approximately $\lambda_{P_U} \approx 1.25\delta_{slot}$ in the polymer-injected trip-upstream case. Furthermore, while notable cycle-to-cycle variations exist, on the average, the shear layer roll-up tends to take place closer to the trip wire in the polymer-injected trip-downstream configuration $[(x - x_{trip})/\delta_{slot} \approx 2 - 3]$ in comparison to the corresponding trip-upstream case, suggesting an increased amplification of velocity perturbations. This leads to an earlier onset of vortex breakdown at $10 < (x - x_{trip})/\delta_{slot} < 15$ in the trip-downstream case. In contrast, the breakdown in both cases considered in the trip-upstream configuration is observed within approximately $25 < (x - x_{trip})/\delta_{slot} < 30$, further suggesting a relatively minor effect of the polymer on the transition process in this configuration.

For a quantitative evaluation of the diffusion of injected polymer in the transitioning boundary layer, time-averaged profiles of normalized polymer concentration are considered in Fig. 4. For consistency, the reference concentration c_{ref} is evaluated immediately downstream of the recirculating region downstream of the trip $[(x - x_{trip})/\delta_{slot} \approx 10.5]$ to minimize inaccuracies caused by the insufficient penetration of the laser sheet through the highly concentrated dye in the separated shear layer. While the polymer concentrations at the chosen reference location are expected to be different in the two cases precluding a quantitative comparison of the near-wall concentration, the normalized concentration profiles in both transitioning cases show a peak in polymer concentration at the wall similar to previous observations in turbulent boundary layers [12,79,87,88]. As expected, the peak magnitudes decrease with increasing streamwise distance due to the wall-normal transport of the polymer noted in Fig. 3.

To aid the quantitative analysis of the effect of the polymer solutions on flow transition, variation of the spatially averaged polymer concentration in the near-wall region is considered in the insets of Figs. 4(a) and 4(b). Spatial averaging is considered in both near-wall viscous region $(0 < y^+ < 30)$

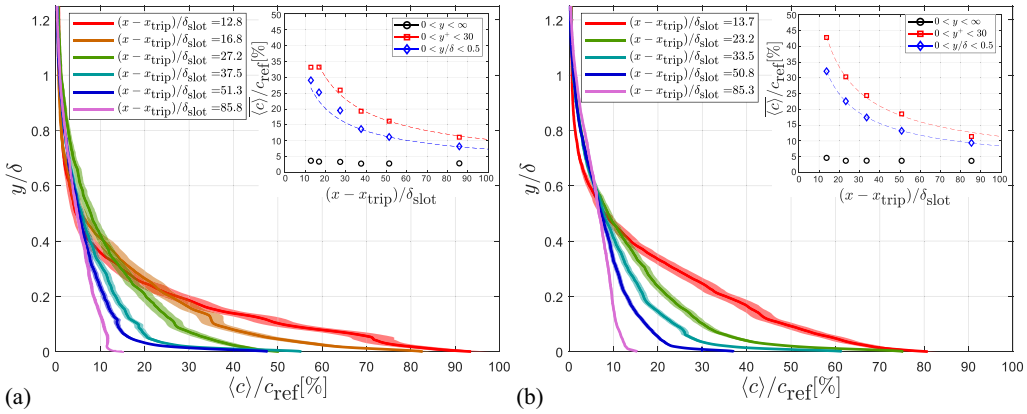

FIG. 4. Profiles of concentration normalized by the concentration of the injected polymer at various downstream distances from the trip wire in the (a) trip-upstream and (b) trip-downstream case. Insets show the variation of spatially averaged concentration ($\overline{\langle c\rangle}/c_{\mathrm{ref}}$) within different regions of the boundary layer with best fits of $\overline{\langle c\rangle}/c_{\mathrm{ref}} \sim (x-x_{\mathrm{trip}})^b$ shown by dashed lines. Variation of $\overline{\langle c\rangle}/c_{\mathrm{ref}}$ computed over the height of the FOV ($0 < y/\delta < \infty$), which exceeds 1.9δ at each location, is shown for reference.

and the lower half of the boundary layer ($0 < y/\delta < 0.5$) to account for the strongly decreasing frictional length scales in the initial portion of the tripped boundary layer (with the scaling parameters estimated using PIV). Results show that the spatially averaged concentrations in the lower half of the boundary layer decrease with the streamwise distance from the trip location according to a power law $\langle c\rangle/c_{\mathrm{inj}} \sim (x-x_{\mathrm{trip}})^b$, with the exponent $b = -0.62$ and -0.67 in the trip-upstream and trip-downstream cases, respectively. The difference between the two cases decreases when the near-wall range ($0 < y^+ < 30$) is considered for spatial averaging, signifying a diminished effect of the trip position on the evolution of the average concentration in the near-wall region.

B. Flow past trip wire

The flow dynamics in the region downstream of the trip wire in each of the cases seen in Fig. 3 is further investigated to offer more quantitative insights into the initial development of the transitional boundary layer. The time-averaged velocity vector field in Fig. 5 confirms the laminar flow separation over the trip wire and the subsequent recirculating region downstream of the trip, as evidenced by the negative streamwise velocity near the wall. The contour corresponding to $\langle u\rangle = 0$, which separates the recirculating region from the streamwise flow, is observed to be aligned with the trip height. Measurements at a downstream location (omitted for brevity) show that the mean flow-field reattaches at approximately $10\delta_{\mathrm{slot}}$ downstream of the trip wire. Similar results are obtained in the baseline flow corresponding to the trip downstream case.

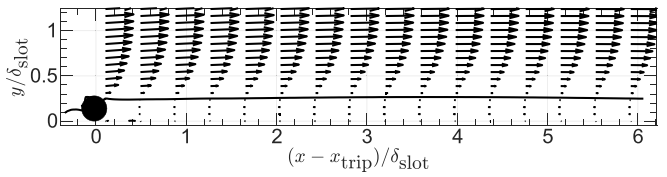

FIG. 5. Time-averaged velocity vectors for the baseline flow showing the recirculation bubble downstream of the trip wire.

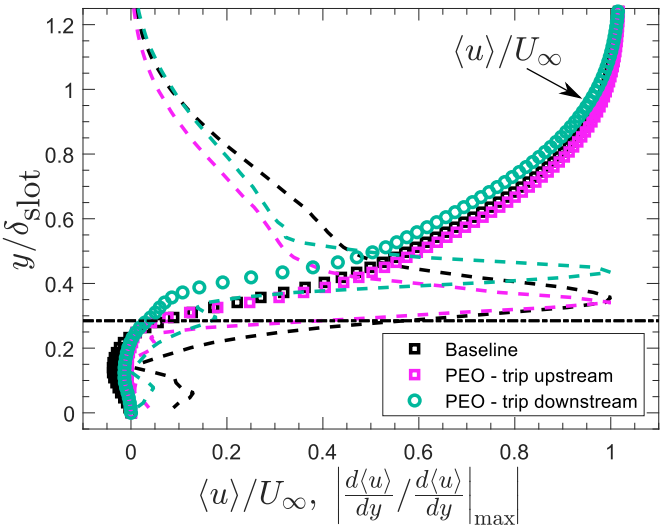

FIG. 6. Time-averaged profiles of streamwise velocity and its gradient with respect to the wall-normal coordinate. Results are averaged within a window of length δ_{slot} downstream of the trip wire. Dash-dot line shows the height of the trip wire.

Time-averaged profiles of streamwise velocity immediately downstream of the trip wire are considered in Fig. 6 to investigate the effect of the polymer on the separated shear layer formed above the recirculating bubble. The results averaged over $0.2 < (x - x_{\mathrm{trip}})/\delta_{\mathrm{slot}} < 1.2$ in each of the presented cases show that, while the recirculating bubble persists in the polymer-injected cases, the magnitude of the negative streamwise velocities within the bubble is notably reduced. This is attributed to the presence of the higher viscosity polymer solutions within the bubble. The results further show that polymer injection in the trip-upstream configuration has a negligible effect on the height of the bubble. In contrast, an increased bubble height, and, thus, the wall-normal distance of the separated shear layer is seen in the trip-downstream configuration, illustrated by the maxima of the normalized wall-normal gradient of the mean streamwise velocity. The difference between the two polymer-injected scenarios may be explained based on the concentration of the polymer contained within the separated shear layer. In the latter configuration, the highly concentrated polymer solution surrounding the upstream portion of the trip-wire experiences relatively strong normal stresses, which are stored within the polymers and are released in the wall-normal (radially outward) direction as they flow past the trip wire into the separated shear layer. This behavior is consistent with the expansion of the wake [89] and earlier separation [90] observed in polymer laden flows over cylinders. Such an imbalance in the normal stresses is not expected to the same degree in the trip-upstream configuration since the polymers are released within the recirculating bubble where significantly lower wall-normal stresses are observed.

To further investigate the development of the separated shear layer formed due to the trip wire and the polymer effect on the resulting transition process, root-mean-square (rms) fields for the streamwise and wall-normal velocities downstream of the trip wire are considered in Fig. 7. The results show relatively large magnitudes of both $u_{\mathrm{rms}}/U_\infty$ and $v_{\mathrm{rms}}/U_\infty$ confined within the boundary layer above the recirculation bubble which is attributed to the rapid growth of perturbations in the separated shear layer. Polymer injection within the recirculation bubble in the trip-upstream configuration marginally lowers the streamwise velocity fluctuations [Fig. 7(b)], while at the same time, increases considerably the wall-normal fluctuations [Fig. 7(e)] within the transitioning shear layer. This effect is notably changed in the polymer-injected trip-downstream configuration which shows substantial magnitudes of $u_{\mathrm{rms}}/U_\infty$ within the shear layer even before it separates from the

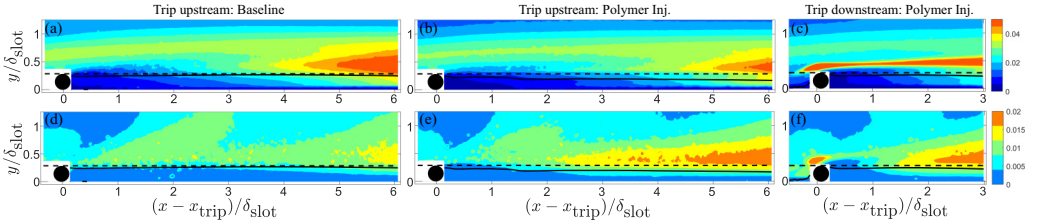

FIG. 7. Normalized rms of the [(a)–(c)] streamwise velocity (u_{rms}/U_∞) and [(d)–(f)] wall-normal velocity (v_{rms}/U_∞) downstream of the trip. Results corresponding to the trip upstream configuration are shown for [(a), (d)] baseline and [(b), (e)] polymer-injected flow, whereas those for the polymer-injected flow in the trip downstream configuration are shown in [(c), (f)]. Dashed lines show the height of the trip and solid lines show the contour corresponding to $\langle u \rangle = 0$.

trip wire along with the region of increased v_{rms}/U_∞ forming closer to the trip wire in comparison to the former case. The strain rates at the upstream periphery of the trip wire are expected to be 10 to 40 times of those expected within the boundary layer [91], and the the corresponding range $10 < \mathrm{Wi} < 100$ pertains to the regime of elasto-inertial flows. The increased streamwise fluctuations within the region confined to the layer of the highly concentrated polymer flow suggests the onset of elastic instabilities which are noted to occur at relatively large Wi and subsequently lead to elasto-inertial turbulence [92,93]. While this phenomenon is not observed in the polymer-injected trip-upstream case, the increased wall-normal fluctuations are indicative of the increased amplification rate of the K-H instability.

The amplification of the shear layer perturbations is further illustrated in Fig. 8. Figures 8(a) and 8(b) present instantaneous snapshot of wall-normal velocity fluctuations showing a distinct periodicity characteristic of K-H instability, with the streamwise wavelength (λ_N) corresponding to that seen in Fig. 3(a)(i). Further, this wavelength is noted to decrease in the polymer-injected flow substantiating the changes in the transition process. Figure 8(c) shows the streamwise variation in rms of the wall-normal fluctuations $v_{rms}|_{y_k}$ sampled along the trip height. The results suggest that polymer-injected flows feature higher amplification rates compared to the baseline flow within $(x - x_{trip})/\delta_{slot} < 2$. For $(x - x_{trip})/\delta_{slot} < 2$, the velocity fluctuations for polymer injected cases reach notably higher levels compared to the baseline case. This is attributed to higher initial amplification rates in polymer-injected cases. With the assumption of exponential amplification, the average initial convective amplification rate of disturbance (σ) can be estimated as $\Delta(\ln(v_{rms}/U_\infty))/(\Delta(x/\delta_{slot}))$ [94], with corresponding fits shown in Fig. 8(c). The resulting estimates for σ are 0.26, 0.57, and 1.25 for baseline, trip-upstream, and trip-downstream cases, respectively. The higher initial amplification rates for the polymer injected flow is likely linked to a strong viscosity wall-normal gradient in the shear layer [95,96]. Further, it is noted that the highest initial amplification rate is observed for the trip-downstream case, which may be attributed to a more pronounced effect of elasto-inertial instabilities in the high strain regions around the trip that act to enhance the transition process. The differences in the convective growth of velocity fluctuations is further demonstrated by comparing the variation of $\int_0^\infty v_{rms} dy/U_\infty \delta_{slot}$ in Fig. 8(d), which serves as an integral measure of velocity fluctuations magnitude in the boundary layer downstream of the trip. The inset in Fig. 8(d) shows that the magnitudes of $\int_0^\infty v_{rms} dy/U_\infty \delta_{slot}$ up to approximately $(x - x_{trip})/\delta_{slot} = 20$, are higher for both polymer injected cases in comparison to the baseline flow, confirming the more rapid transition process inferred from Fig. 8(c). However, a notable decay in the integral amplitude of fluctuations is observed farther downstream for both polymer cases. This is believed to be the result of polymer activation by significant turbulent stresses developing in the late stages of transition, and the associated transitional flow development and characteristics are discussed in more detail in the next section.

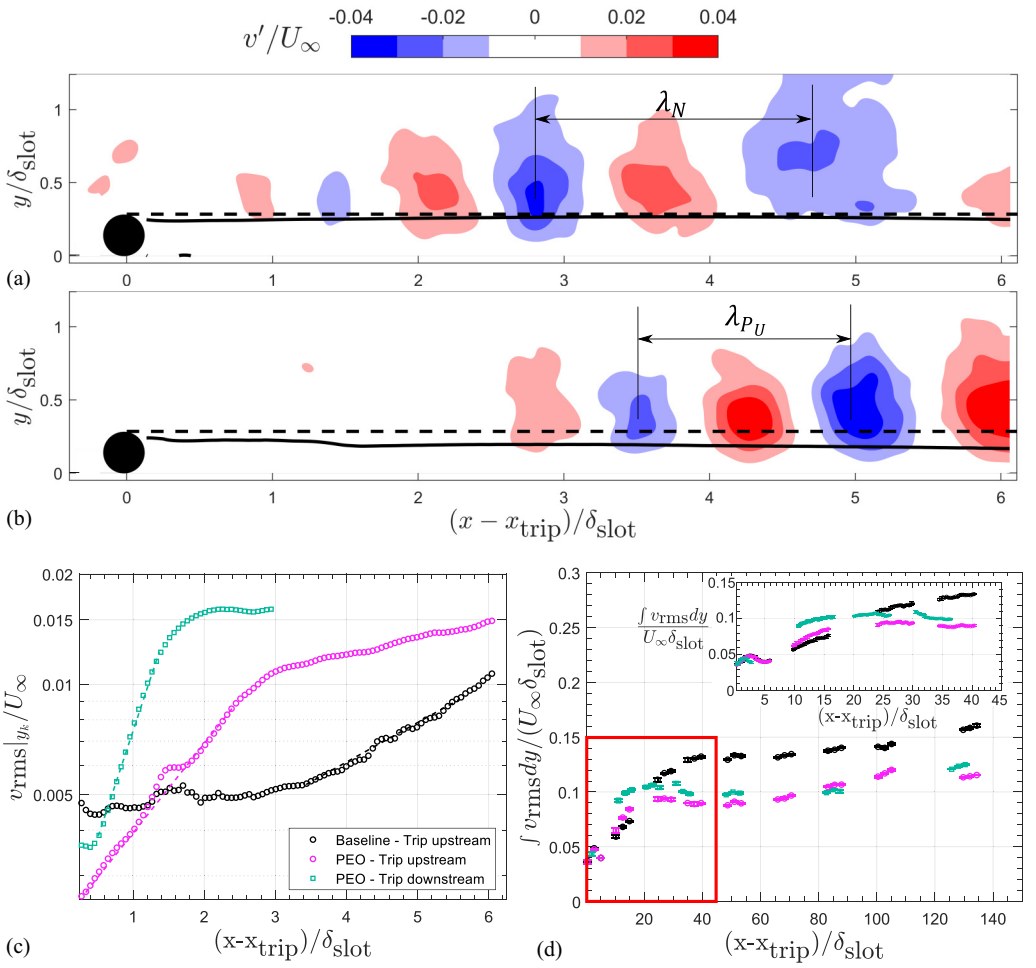

FIG. 8. Representative instantaneous realizations showing vortex shedding in (a) baseline and (b) polymer-injected trip-upstream cases. Contours are smoothed with a two-dimensional Gaussian window ($0.25\delta_{\text{slot}} \times 0.25\delta_{\text{slot}}$). Black dashed lines show the height of the trip, and solid lines show the contour corresponding to $\langle u \rangle = 0$. (c) The variation of v_{rms} with $(x - x_{\text{trip}})/\delta_{\text{slot}}$ at the height of the trip y_k. (d) Variation of $\int_0^\infty v_{\text{rms}} dy/U_\infty \delta_{\text{slot}}$ with $(x - x_{\text{trip}})/\delta_{\text{slot}}$, and the inset in (d) shows a zoomed-in view of the region covering $0 < (x - x_{\text{trip}})/\delta_{\text{slot}} < 45$, which is highlighted in red.

C. Transitional flow development

The quantitative description of the development of the transitional boundary layer induced by the trip is first considered through the variation in the boundary layer parameters in the streamwise direction in Fig. 9. Results are complemented with the variation in the boundary layer parameters corresponding to the no-trip configuration (laminar flow) in the left column of Fig. 9 for reference. Figure 9(a) shows the expected variation in both boundary layer thickness (δ) and displacement thickness (δ^*) in the baseline flow, and the effect of water injection is seen to be negligible on these parameters. Similar results are noted for the shape factor (H) for these two cases, with H remaining close to the expected value of 2.6 in the laminar boundary layer and decreasing marginally with increasing streamwise distance. The marginal decrease in H is attributed to the natural amplification of the disturbances within the laminar boundary layer expected to occur at Re_{δ^*} greater than $\text{Re}_{\text{crit}} = 520$ (Table I). The polymer injection produces a notable increase in all

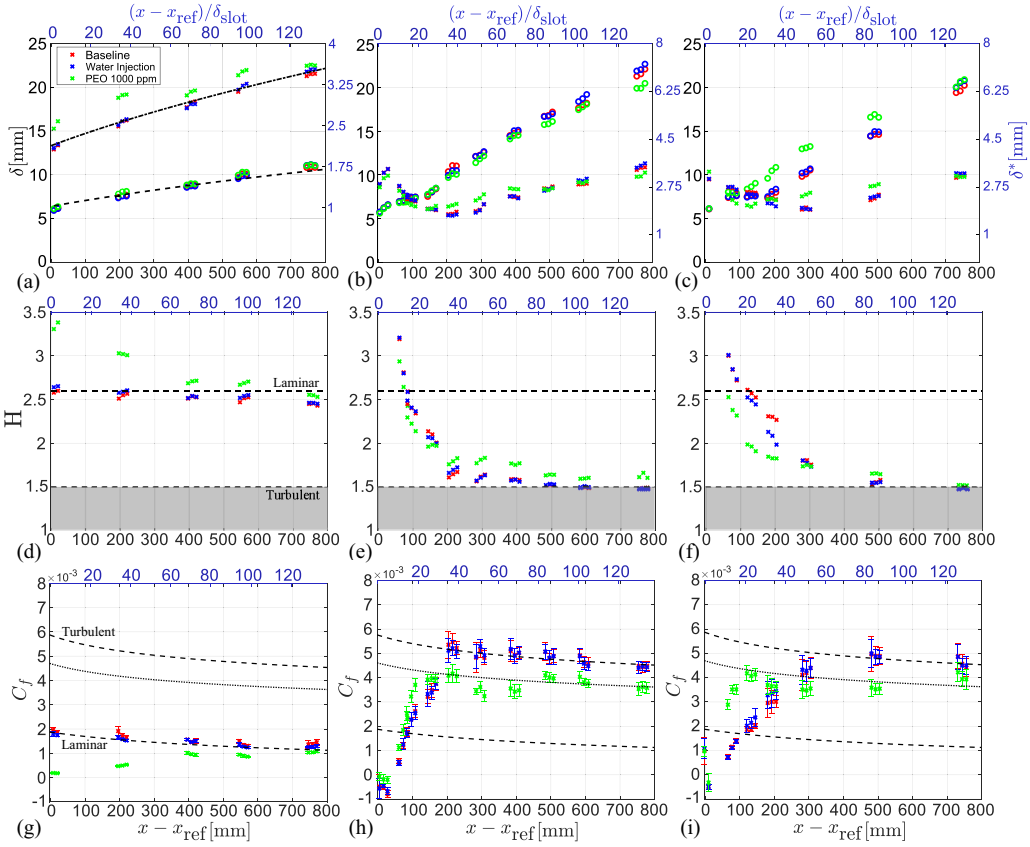

FIG. 9. Variation of the boundary layer parameters in [(a), (d), (g)] no-trip (laminar), [(b), (e), (h)] trip-upstream, and [(c), (f), (i)] trip-downstream configurations. Left axis in the top row shows the variation of boundary layer thickness (δ) marked by $\circ$, and right axis shows displacement thickness (δ^*) marked by $\times$. Middle row shows the shape factor $H = \delta^*/\theta$, and bottom row shows the skin friction coefficient C_f. Black dashed and dash-dotted lines in (a) show the typical variation in laminar boundary layers from Blasius' relations, and dashed lines in (d)–(i) indicate typical values of H and C_f in laminar and turbulent boundary layers as indicated. Dotted line in (g)–(i) shows 20% reduction in C_f from the Prandtl-Kármán (turbulent) law. Reference location x_{ref} is considered at the injection slot (x_{inj}) in the no-trip configuration and at the trip wire (x_{trip}) in the tripped boundary layer cases.

the boundary layer parameters close to the injection slot, but this effect is seen to progressively decrease with increasing streamwise coordinate. The increase in δ^*, and consequently H, close to the injection slot is consistent with the observations in polymer-injected turbulent boundary layers [12] and is attributed to the decreased near-wall streamwise velocity due to the higher viscosity within the concentrated layer of polymer formed close to the wall (Fig. 4).

As expected, the introduction of the trip wire results in a significant increase in the boundary layer thickness compared to the laminar flow in both transitional cases [Figs. 9(b) and 9(c)]. On the other hand, the displacement thickness decreases initially in the range $(x - x_{\mathrm{trip}})/\delta_{\mathrm{slot}} < 50$ ($x - x_{\mathrm{trip}} < 300$ mm) before increasing monotonically. This initial decrease in δ^* has also been noted [48] in transitional boundary layers and is attributed to the increased mass flow rate within the boundary layer caused by the increased mixing of the outer flow by growing perturbations. Compounded by the increase in the momentum thickness (θ), the shape factor decreases sharply within $(x - x_{\mathrm{trip}})/\delta_{\mathrm{slot}} < 50$ from the value of 2.6, followed by a more gradual decrease until the boundary layer becomes fully turbulent [Figs. 9(e) and 9(f)]. The decrease in H in the latter

portion of transition region [$(x - x_{\text{trip}})/\delta_{\text{slot}} > 50$] is mainly driven by the increase in the momentum thickness, as δ^* increases in this range. It is further observed that the boundary layer thickness in the trip-downstream case is lower than the case where the trip is positioned upstream of the injection slot. This is attributed to a decreased effectiveness of the trip in the former case as a result of the lower Re_k at the trip wire. Furthermore, these trends are seen to hold with the injection of water, indicating that the effect of benign injection is negligible.

In the trip-upstream configuration, the polymer injection is seen to produce a minor effect on the development of the boundary layer thickness with more notable changes seen in the latter portion of transition and in the turbulent regimes [Fig. 9(b)]. In contrast, the δ^* is reduced below the corresponding Newtonian values immediately downstream of the trip, while it is increased at the locations near the minimum in δ^* ($(x - x_{\text{trip}})/\delta_{\text{slot}} \approx 35$), indicating reduced turbulent mixing by the polymers leading to a decreased mass flow rate within the boundary layer. This is further seen from the sharper reduction of H in the region $(x - x_{\text{trip}})/\delta_{\text{slot}} < 35$ in comparison to the corresponding Newtonian values. For $(x - x_{\text{trip}})/\delta_{\text{slot}} > 35$, the decrease in the shape factor saturates and progresses at a rate lower than that in the Newtonian flow indicating the activation of the polymer effect.

Unlike the results seen with the trip-upstream configuration, the boundary layer thickness for the polymer injected transitional boundary layer in the trip-downstream case [Fig. 9(c)] is notably increased in comparison to the corresponding Newtonian flows at $(x - x_{\text{trip}})/\delta_{\text{slot}} < 35$. This is attributed to the increased amplification of the instabilities closer to the trip wire, which results in an earlier breakdown to turbulence as previously shown in Figs. 3 and 7. These effects are confirmed by the significantly decreased values of δ^* and H in $(x - x_{\text{trip}})/\delta_{\text{slot}} < 35$. Beyond this range, both δ^* and H are seen to be higher than the corresponding values in the Newtonian cases, suggesting the polymer action to be effective in controlling turbulence. However, H is seen to progressively decrease to typical values in turbulent Newtonian flows towards the end of the measurement domain which is attributed to the progressive depletion of the near-wall polymer concentration (Fig. 4).

The results for the no-trip case in Fig. 9(g) confirm that the variation of C_f follows the canonical trends in laminar boundary layers. As expected, the relatively viscous layer formed by the injected polymer solution close to the wall results in a decreased gradient of the streamwise velocity at the wall ($d\langle u\rangle/dy|_w$) as noted from the figure. However, it must be noted that the actual C_f is higher than that for the baseline flow of water given that the polymer solutions exhibit a shear viscosity that is an order of magnitude higher than the viscosity of water at the employed shear rates [11,12]. With the addition of the trip wire [Figs. 9(h) and 9(i)] and the subsequent creation of the recirculating bubble, negative values of C_f are observed immediately downstream of the trip. As the flow develops downstream, the C_f is seen to monotonically increase and then converge on the trend predicted by the Prandtl-Kármán law for the fully turbulent boundary layer, in accordance with previous studies on bypass transition [28,48,97]. The location where the peak in C_f is obtained is usually denoted as the *transition point* [98]. As observed in Fig. 9, the differences in the transitional flows between the two trip position cases considered here are also seen in the variation of C_f, highlighting the sensitivity of the trip effectiveness to Re_k. Due to a lower Re_k, the transition point is noted to occur later in the trip-downstream configuration, i.e., in the range $70 < (x - x_{\text{trip}})/\delta_{\text{slot}} < 85$, whereas it occurs in the range $30 < (x - x_{\text{trip}})/\delta_{\text{slot}} < 40$ in the trip-upstream configuration. Further, consistent with the results for other boundary layer parameters, on the average, water injection is not seen to significantly alter the flow development.

Figures 9(h) and 9(i) show a notable effect of polymer injection on the variation of C_f in the transitional flows. While the general trend in the variation of C_f agrees with the Newtonian cases, the C_f is noted to be significantly higher than the corresponding Newtonian values in the initial part of the transition process. This agrees with the earlier observations of the enhanced transition by the polymer injection and the associated trends in C_f are attributed to the insufficient activation of the polymers in this region. The C_f is seen to peak at similar values in both polymer-injected transitional flows, but at lower values than the peak in the corresponding Newtonian flows. The decreased magnitude of the peak C_f is attributed to the *onset* of polymer activation, which likely occurs

upstream of the peak leading to a progressively increasing suppression of the turbulent motions, as expected from previous studies in drag-reduced internal flows [7]. This leads to an earlier saturation in the initially more rapid growth of C_f in the polymer-injected cases. Similar to that in the Newtonian flows, the location where the peak C_f occurs in the polymer-injected cases may be regarded as the transition point, however, in contrast to Newtonian flows, the polymer-laden flow beyond this point is not expected to be representative of a fully developed turbulent flow. This point is found to occur at a similar distance from the trip in comparison to the corresponding Newtonian flow in the trip-upstream configuration, i.e., in the range $25 < (x - x_{\text{trip}})/\delta_{\text{slot}} < 40$, whereas it is notably advanced closer to the trip in the polymer-injected trip-downstream configuration, i.e., in the range $15 < (x - x_{\text{trip}})/\delta_{\text{slot}} < 30$ in comparison to the corresponding Newtonian flow.

In both trip configurations, the skin friction growth saturates at the values lower than those for the corresponding baseline Newtonian flows and show drag reduction in the developing turbulent boundary layer. For example, Fig. 9(h) shows that the local drag reductions (DRs) are at least 20% for a considerable distance beyond the transition point for the trip-upstream configuration, where DR is given as

$$\text{DR}[\%] = 100 \times \frac{C_{f_N} - C_{f_P}}{C_{f_N}}, \tag{1}$$

with C_{f_N} and C_{f_P} being the local skin friction coefficients in the baseline Newtonian and polymer-injected cases, respectively. Due to the diffusion of the near-wall polymer (Fig. 4), the DR progressively decreases, and the C_f values are seen to gradually return towards to the corresponding Newtonian values within the drag-reduced regime of the transitional flow. Similar results are noted in the case with the trip positioned downstream of the injector [Fig. 9(i)]; however, the effect is seen to diminish at a higher rate which is partially attributed to the relatively higher diffusion rate of the average near-wall polymer concentration (Fig. 4). It is noted that the DR obtained in both polymer injected transitioning scenarios in the present study is lower than that expected in a fully developed turbulent boundary layer at comparable values of the K parameter and the injected concentrations, where $K = c_{\text{inj}} Q_{\text{inj}}/\rho(x - x_{\text{inj}})U_\infty$ [80] due to a lower shear rate and reduced mixing of the injected polymer solution within the boundary layer.

In order to facilitate a more effective comparison between the two different trip placement configurations, variation of H and C_f with the frictional Reynolds number (Re_τ) is considered in Fig. 10. The figure also reproduces data from the T3A and T3B cases from Roach and Brierley [28] as a reference. Although their study was performed in transitioning boundary layers bypassed using high freestream turbulence intensities, the Re_τ obtained by Roach and Brierley are similar to the ones employed in the present study. Figures 10(a) and 10(b) show an excellent agreement in the shape factor data of the present results and the reference in the later stages of transition, while the differences in the earlier transition stages are attributed to the different methods used to induce the bypass transition in the two studies. The collapse between the tripped cases considered in the present study with those from Roach and Brierley [28] highlights the universality of the variation in H in the late transitional stages. As suggested by Dhawan and Narasimha [48], this universality is associated with the late transition stages being dominated by turbulent spots, independent of the mechanism by which transition has been initiated. Furthermore, the results for the polymer-injected flows are also found to be in agreement with the Newtonian flows, highlighting self-similarity between these flows in terms of Re_τ. This self-similarity facilitates extrapolations for the streamwise distances required for the drag-reduced transitional flows to reach fully turbulent states expected at $H = 1.5$ or $\text{Re}_\tau \approx 300$, and the present results exhibit an effective delay in reaching the fully turbulent state in the polymer-injected flows. A similar result is noted in the variation of C_f [Figs. 10(c) and 10(d)], which shows a collapse of both Newtonian and polymer-injected flows with the T3B case in the transition regime. Furthermore, the rate of increase of C_f with Re_τ is found to be approximately equal between the two trip configurations investigated in the present study, despite the noted differences in the trip effectiveness and polymer performance between these cases.

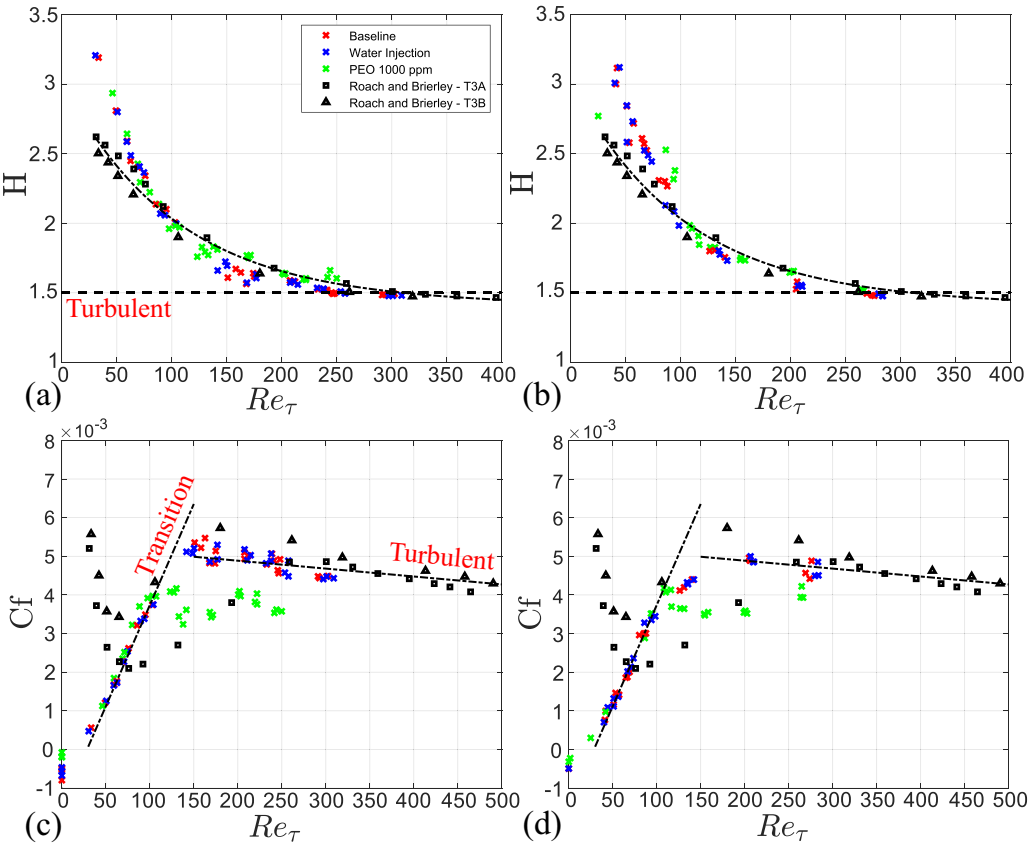

FIG. 10. Variation of the shape factor (H) and the skin friction coefficient (C_f) in [(a), (c)] trip-upstream, and [(b), (d)] trip-downstream cases with Re_τ. Data corresponding to the T3A and T3B cases from the study of Roach and Brierley [28] are included for reference. Dash-dotted lines in (a) and (b) show best fits to the T3A and T3B cases, and dashed line indicates the typical value in fully developed turbulent boundary layers. Dash-dotted lines in (c) and (d) show linear fits to the data corresponding to the transition and turbulent regimes as indicated.

To further aid the understanding of the transitional flow development, time-averaged profiles of the streamwise velocity are considered in inner coordinates in Fig. 11. An equivalent Re_{τ_0} in the baseline flow in each of the cases is indicated to aid the comparisons between the two tripped configurations. The figure shows that beyond the initial region of decreased near-wall streamwise momentum caused by the wake of the trip wire ($\mathrm{Re}_{\tau_0} < 150$), the baseline and water-injected Newtonian cases exhibit the expected progression towards a logarithmic profile in the fully developed turbulent flow seen at $\mathrm{Re}_\tau \approx 300$. A similar development is seen in the polymer-injected cases as the flow develops past the initial trip effects. The profiles at $\mathrm{Re}_{\tau_0} > 150$ closely follow the expected trends in a drag-reduced turbulent boundary layer with the developed logarithmic region shifted vertically from the Newtonian log-law depending on the achieved DR as shown by previous studies [12,80,99]. The disparities in the development of the velocity profiles in the earlier stages of the transition between the two configurations are attributed to the earlier noted differences in the initial transition process and near-wall polymer distribution between the two cases.

Time-averaged profiles of Reynolds normal and shear stresses in inner coordinates are considered in Fig. 12 with increasing Re_{τ_0}. Close to the trip wire, i.e., at $\mathrm{Re}_{\tau_0} < 100$, the results show substantial magnitudes for all the Reynolds stresses within $y^+ < 30$ which is attributed to the amplification of

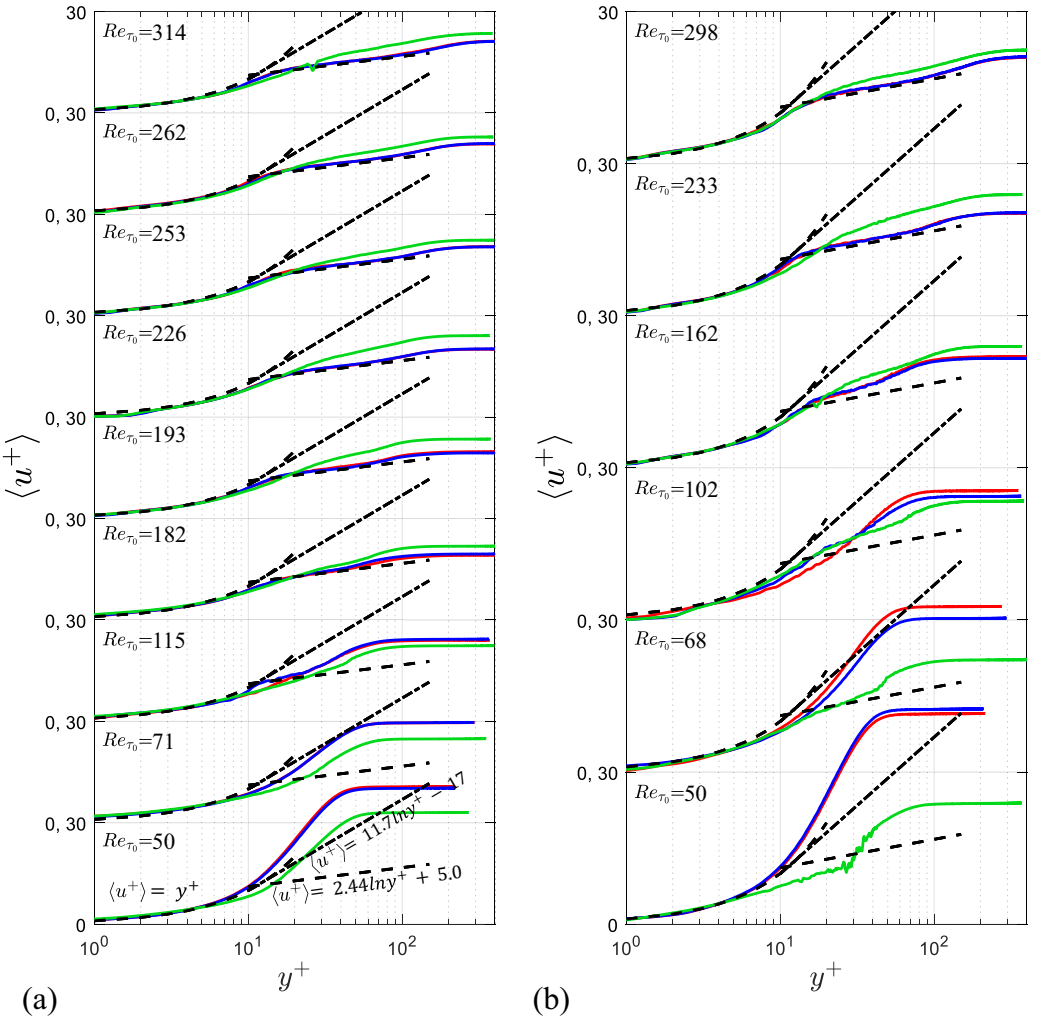

FIG. 11. Mean streamwise velocity profiles in inner coordinates for (a) trip-upstream and (b) trip-downstream case. Profiles are displaced vertically to distinguish the streamwise positions marked by Re_{τ_0}. Color coding for the various cases follows the one shown in Fig. 10. Black-dashed lines indicate the near-wall and logarithmic laws in turbulent boundary layers and dash-dotted lines show Virk's MDR profile.

K-H instability and the subsequent shedding of vortical structures in this region. Comparatively lower peak magnitudes are observed in this region for the trip-downstream configuration due to a lower tripping efficiency (lower Re_k) in this tripping scenario. As the vortices breakdown farther downstream ($\mathrm{Re}_\tau > 100$), a peak in $\langle u'u' \rangle$ develops at $y^+ \approx 15$ and grows in both transitional scenarios, aligned with the results expected in the limiting case of fully developed turbulent boundary layers. Similarly, both $\langle v'v' \rangle$ and $-\langle u'v' \rangle$ peak farther away from the wall from a relatively early stage of transition in both configurations and reach their respective expected peak values in the limiting case by $\mathrm{Re}_{\tau_0} \approx 200$. Furthermore, the profiles of both $\langle u'u' \rangle$ and $\langle v'v' \rangle$ corresponding to the Newtonian flow agree with the results of the T3A case from Roach and Brierley [28] in the late transition stages, signifying the aforementioned universality in the flow development.

Although a similar development of the profiles of the Reynolds stresses is seen in the polymer-injected transitional flows, notable differences in the peak magnitudes and locations are seen with

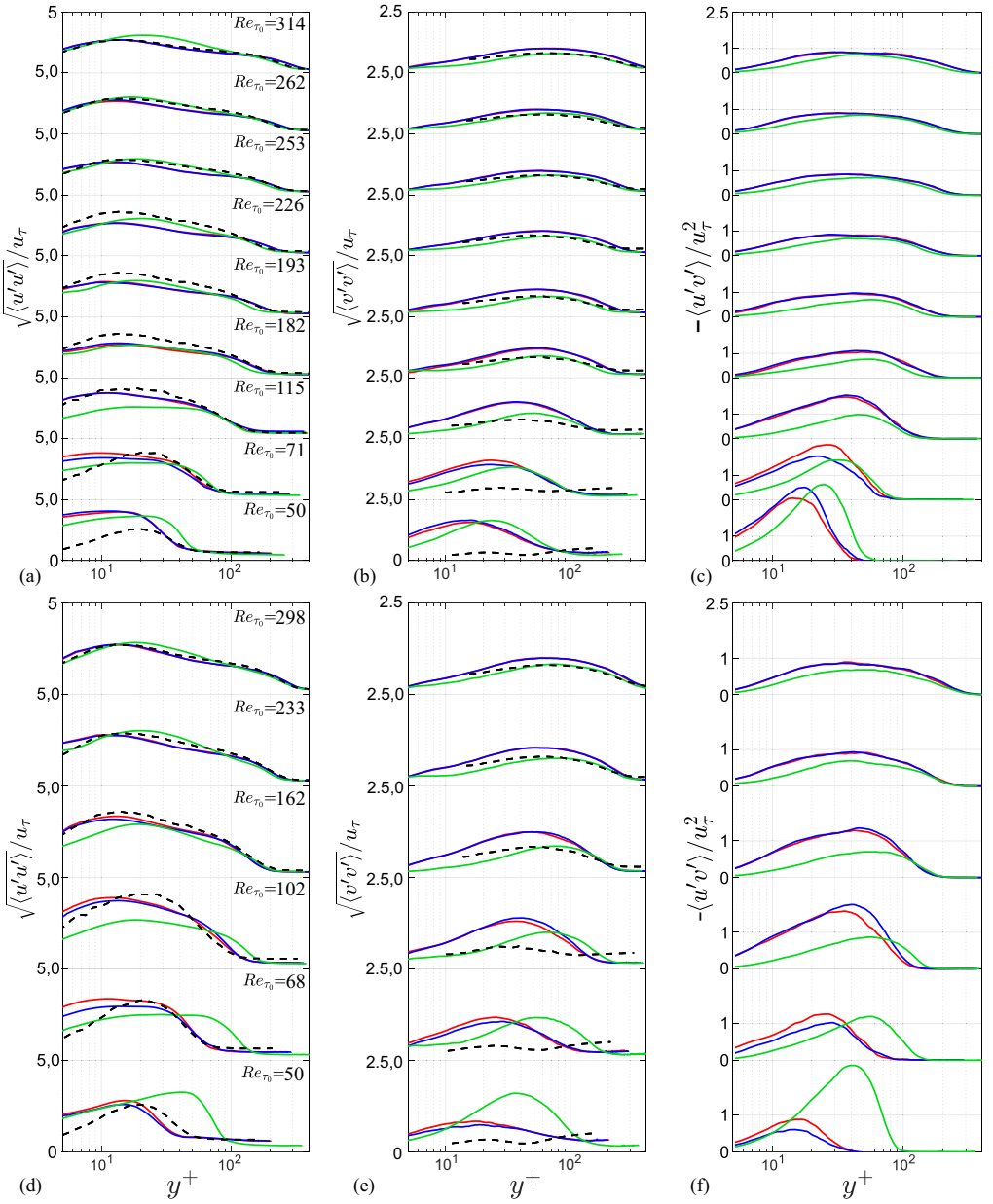

FIG. 12. Reynolds normal and shear stresses in inner coordinates for [(a)–(c)] trip-upstream and [(d)–(f)] trip-downstream case. Profiles are displaced vertically to distinguish the streamwise positions marked by Re_{τ_0} in the left column. Color coding for the various cases follows the one shown in Fig. 10. Black dashed profiles are shown at equivalent friction Reynolds numbers from the T3A case of Roach and Brierley [28].

respect to the corresponding Newtonian profiles. Moreover, the differences are considerable in the early transition stages ($\mathrm{Re}_{\tau_0} < 100$) between the two transitional flows. The latter is attributed to a rapid transition process due to a relatively high shear and the resulting amplification of the instabilities within the separated shear layer in the trip-downstream configuration. As the

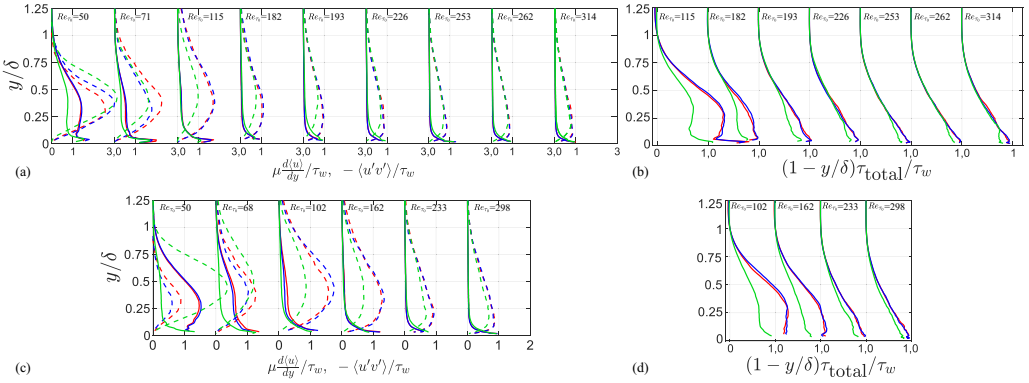

FIG. 13. Variation of the viscous ($\mu d\langle u\rangle/dy$) and Reynolds shear stress ($-\rho\langle u'v'\rangle$) in outer coordinates for (a) trip-upstream and (c) trip-downstream case. Variation of the total stress multiplied by $(1-y/\delta)$ for the respective cases in shown in (b) and (d) following Hou *et al.* [100]. Stresses are normalized by the respective wall-shear stress (τ_w) in each of the cases. Profiles are displaced horizontally to distinguish the streamwise positions marked by Re_{τ_0}. Dashed lines in (a) and (c) represent Reynolds shear stress, and solid lines show the viscous stress. Total stress profiles ($(1-y/\delta)\tau_{\text{total}}$) are shown only for the later stages of the transitioning boundary layer as indicated by the top axis. Color coding for the various cases follows the one shown in Fig. 10.

flow proceeds towards the late transition stages ($\text{Re}_{\tau_0} > 100$), the polymer effect is seen to reduce the near-wall turbulent fluctuations in all Reynolds stresses, while increasing the $\langle u'u'\rangle$ above the Newtonian values in the buffer and lower-log regions ($20 < y^+ < \delta^+/2$), in alignment with the behavior expected in drag-reduced turbulent boundary layers [12,80,101]. Further, following the behavior in the limiting case of turbulent boundary layers, the peaks in all the Reynolds stresses appear to shift in the wall-normal direction in the late transition stages, indicating the formation of a thicker buffer layer.

The efficiency of the polymers within the boundary layer is directly observed by considering the normalized profiles of the total shear stress (τ_{total}), which is composed of the Reynolds shear stress ($-\rho\langle u'v'\rangle$) and the viscous stress ($\mu d\langle u\rangle/dy$) as illustrated in Fig. 13. Since the normalized stress components are significantly higher in the early transition stages, and they develop towards their limiting values in the late transitional stages, as illustrated in Figs. 13(a) and 13(c), the normalized profiles of τ_{total} are considered for $\text{Re}_{\tau_0} > 100$. Following the approach of Hou *et al.* [100], the normalization by the local wall-shear stress ($\tau_w = \rho u_\tau^2$) and weighting by $(1-y/\delta)$ allows for an evaluation of the polymer stress (τ_P). The results in Figs. 13(b) and 13(d) corresponding to the two transitional cases investigated in this study indicate a collapse of the weighted data on a linear trend within $0 < y/\delta < 0.6$ as expected in turbulent Newtonian flows. Further, the weighted profiles for the polymer-injected flow are also seen to collapse on the same trend in the outer layer of the boundary layer with a progressively decreasing stress deficit which is attributed to the decreasing polymer concentration in the near-wall region. While the self-similar linear trend of the weighted total stress profiles is not observed in the early-to-midtransitional regime precluding a quantitative assessment of the polymer stresses in this region, the results qualitatively show a significant accumulation of the polymer stresses throughout the boundary layer thickness. Comparison of the stress deficits between the two tripping configurations suggests that considerable polymer stresses are accumulated and maintained farther away from the wall in the trip-downstream case owing to a relatively larger wall-normal polymer transport close to the trip (Fig. 4) leading to a broader polymer-affected region.

IV. CONCLUSION

The present study investigates experimentally the effect of slot-injected polymer (1000 ppm of polyethylene oxide) on laminar-to-turbulent transition in flat-plate tripped boundary layers using a two-dimensional trip wire. The resulting transitioning boundary layer is characterized using planar PIV and PLIF measurements which allow for a detailed study of the streamwise development of the bypass transition process. Further, the study explores the effectiveness of polymer injection for two different trip placements relative to the injection slot. For the trip positions upstream of the slot ($\mathrm{Re}_k = 229$ based on the trip height), the polymer is injected within a recirculating bubble formed downstream of the trip wire (trip-upstream configuration). For the trip positioned downstream of the injector ($\mathrm{Re}_k = 210$), the polymer is injected in the laminar boundary layer upstream of the trip (trip-downstream configuration). The results provide a detailed understanding of the salient flow features and elucidate the potential advantages and drawbacks of polymer injection in the considered configurations which are critical for the practical implementation of this flow control technique on various marine vehicles.

The mean flow in the region downstream of the trip elicits an inflectional streamwise velocity profile due to the formation of a long recirculating region (approximately $10\delta_{\mathrm{slot}}$). Accordingly, this leads to a relatively rapid amplification of Kelvin-Helmholtz instabilities within the separated shear layer which is illustrated using both flow visualization and quantitative measurements. In both trip-slot configurations, a more accelerated transition is induced by the polymer injection in comparison to the corresponding Newtonian base flow, which is attributed to the strong wall-normal viscosity gradient induced in the shear layer due to polymer injection. The polymer injection within the laminar flow region upstream of the trip wire (trip-downstream case) results in a more rapid amplification of perturbations and consequently an earlier breakdown to turbulence compared to the trip-upstream case. This is likely a result of more pronounced elasto-inertial instabilities resulting from higher polymer deformations induced in the higher strain regions around the trip wire. Additionally, the confinement of the polymer solution within the separated shear layer in conjunction with the larger wall-normal fluctuations closer to the trip wire in the trip-downstream case results in a discernible increase in polymer diffusion in the lower half of the boundary layer.

While the results highlight a counterproductive effect of the polymer injection on the bypass transition, reflected in the decreased shape factors (H) and increased C_f, the peak C_f attained at the transition point is lower than that in the corresponding Newtonian flow. The ensuing flow downstream of the transition point elicits drag reduction related to the near-wall polymer concentration, highlighting the onset of the drag reduction phenomenon within the late transition stages. In this regard, the critical shear stress corresponding to the onset of drag reducing effect is observed to be nearly equal in the two tripped cases considered in the present study while the drag-reduced regime persists over a longer streamwise distance in the trip-upstream scenario due to a relatively higher near-wall polymer concentration. Although the differences in the tripping efficiency in the considered cases result in varying trends in the outer coordinates, consideration of the variation of both H and C_f with Re_τ is observed to be in excellent alignment with the results of Roach and Brierley [28], illustrating a universal behavior in the late transition stages irrespective of polymer injection or the mechanism by which bypass transition is initiated.

In accordance with the noted universality in the late transition stages, the time-averaged profiles of streamwise velocity and Reynolds stresses show a consistent progression towards those expected in the limiting fully developed turbulent flow from the mid-to-late stages of transition ($\mathrm{Re}_{\tau_0} > 150$). Barring the differences in the early stages of transition, similar progression is seen in the polymer injected flow relative to the corresponding expectations in the drag-reduced turbulent boundary layer flow. Further, the development of the profiles of total stress elicits a self-similar behavior in the outer layer in both Newtonian and drag-reduced flow. A progressively decreasing stress deficit in both magnitude and wall-normal coverage is observed in the polymer-injected cases, which is attributed to the declining drag reduction and polymer stress accumulation closer to the wall.

In the context of a practical implementation of this flow control strategy on marine vehicles, the present results, when considered in conjunction with the results in polymer injected turbulent boundary layers (e.g., Shah and Yarusevych [12]), suggest that the polymer effect is activated in the late transition stages and fully turbulent regime. The higher turbulent intensity in the late transition stages causes an effective mixing of the viscous polymer layer with the base medium leading to drag reduction within $x - x_{\text{trip}} < 20\delta_{\text{tr}}$ [12], whereas the onset of drag reduction is delayed to $x - x_{\text{trip}} > 40\delta_{\text{tr}}$ with the injection in the earlier transition stages seen in the present study. In this regard, a critical shear stress is observed to be applicable for the activation of the polymer effect, which is reached late in the transition process making the corresponding region more suitable for polymer injection. This will also help mitigate the advancement of transition and the associated increase in skin friction caused by polymer injection in the laminar boundary layer.

ACKNOWLEDGMENTS

The authors gratefully acknowledge the Natural Sciences and Engineering Research Council of Canada (NSERC) Award/Contract No. RGPIN-04222 for funding of this work.

[1] R. Sellin, J. Hoyt, and O. Scrivener, The effect of drag-reducing additives on fluid flows and their industrial applications part 1: Basic aspects, J. Hydraul. Res. **20**, 29 (1982).
[2] R. Sellin, J. Hoyt, J. Poliert, and O. Scrivener, The effect of drag reducing additives on fluid flows and their industrial applications part 2: Present applications and future proposals, J. Hydraul. Res. **20**, 235 (1982).
[3] H. Canham, J. Catchpole, and R. Long, Boundary layer additives to reduce ship resistance, Naval Architect J. Rina. 87 (1971).
[4] B. Doherty, Investigation of drag reduction obtained through boundary layer injection of dilute solutions of poly (ethylene-oxide), Tech. Rep., US Naval Academy, Annapolis, MD (1965).
[5] R. Sellin, Drag reduction in sewers: First results from a permanent installation, J. Hydraul. Res. **16**, 357 (1978).
[6] N. C. Franz, Fluid additives for improving high velocity jet cutting, in *Proc. First International Symposium on Jet Cutting Technology*, paper A7 (BHRA Fluid Engineering, Cranfield, 1972), pp. 93—-104.
[7] P. S. Virk, Drag reduction fundamentals, AIChE J. **21**, 625 (1975).
[8] J. L. Lumley, Drag reduction by additives, Annu. Rev. Fluid Mech. **1**, 367 (1969).
[9] C. M. White and M. G. Mungal, Mechanics and prediction of turbulent drag reduction with polymer additives, Annu. Rev. Fluid Mech. **40**, 235 (2008).
[10] L. Xi, Turbulent drag reduction by polymer additives: Fundamentals and recent advances, Phys. Fluids **31**, 121302 (2019).
[11] S. Shaban, M. Azad, J. Trivedi, and S. Ghaemi, Investigation of near-wall turbulence in relation to polymer rheology, Phys. Fluids **30**, 125111 (2018).
[12] Y. Shah and S. Yarusevych, Streamwise evolution of drag reduced turbulent boundary layer with polymer solutions, Phys. Fluids **32**, 065108 (2020).
[13] Y. Shah, S. Ghaemi, and S. Yarusevych, Three-dimensional characterization of Reynolds shear stress in near-wall coherent structures of polymer drag reduced turbulent boundary layers, Exp. Fluids **62**, 166 (2021).
[14] M. Warholic, D. Heist, M. Katcher, and T. Hanratty, A study with particle-image velocimetry of the influence of drag-reducing polymers on the structure of turbulence, Exp. Fluids **31**, 474 (2001).
[15] C. White, V. Somandepalli, and M. Mungal, The turbulence structure of drag-reduced boundary layer flow, Exp. Fluids **36**, 62 (2004).
[16] Y. Dubief, C. M. White, V. E. Terrapon, E. S. Shaqfeh, P. Moin, and S. K. Lele, On the coherent drag-reducing and turbulence-enhancing behaviour of polymers in wall flows, J. Fluid Mech. **514**, 271 (1999).

[17] K. Kim, C.-F. Li, R. Sureshkumar, S. Balachandar, and R. J. Adrian, Effects of polymer stresses on eddy structures in drag-reduced turbulent channel flow, J. Fluid Mech. **584**, 281 (2007).
[18] A. S. Pereira, G. Mompean, L. Thais, and R. L. Thompson, Statistics and tensor analysis of polymer coil–stretch mechanism in turbulent drag reducing channel flow, J. Fluid Mech. **824**, 135 (2017).
[19] T. Min, J. Y. Yoo, H. Choi, and D. D. Joseph, Drag reduction by polymer additives in a turbulent channel flow, J. Fluid Mech. **486**, 213 (2003).
[20] W. S. Saric, H. L. Reed, and E. J. Kerschen, Boundary-layer receptivity to freestream disturbances, Annu. Rev. Fluid Mech. **34**, 291 (2002).
[21] W. M. Orr, The stability or instability of the steady motions of a perfect liquid and of a viscous liquid. Part ii: A viscous liquid, Proc. R. Irish Acad. A **27**, 69 (1907–1909).
[22] A. Sommerfeld, Ein Beitrag zur hydrodynamischen Erklärung der turbulenten Flüssigkeitsbewegung, in *4th Int. Congr. Math. III, Rome, Italy*, edited by G. Castelnuovo (1908), pp. 116–124.
[23] H. L. Reed, W. S. Saric, and D. Arnal, Linear stability theory applied to boundary layers, Annu. Rev. Fluid Mech. **28**, 389 (1996).
[24] G. B. Schubauer and H. K. Skramstad, Laminar-boundary-layer oscillations and transition on a flat plate, Tech. Rep., National Aeronautics and Space Administration, Washington DC (1948).
[25] W. S. Saric, J. A. Hoos, and R. H. Radeztsky, Boundary-layer receptivity of sound with roughness, in *Boundary Layer Stability and Transition to Turbulence* (1991), p. 17.
[26] W. S. Saric, Physical description of boundary-layer transition: Experimental evidence, in AGARD (1994).
[27] M. V. Morkovin, Bypass-transition research: Issues and philosophy, in *Instabilities and Turbulence in Engineering Flows* (Springer, 1993), pp. 3–30.
[28] P. Roach and D. Brierley, The influence of a turbulent free-stream on zero pressure gradient transitional boundary layer development: Part 1. Test cases T3A and T3B, in *ERCOFTAC Workshop, Lausanne, 1990* (1990).
[29] M. Matsubara and P. H. Alfredsson, Disturbance growth in boundary layers subjected to free-stream turbulence, J. Fluid Mech. **430**, 149 (2001).
[30] F. Lundell, Experimental studies of bypass transition and its control, Ph.D. thesis, KTH, Stockholm, 2003.
[31] E. Reshotko, Disturbances in a laminar boundary layer due to distributed surface roughness, in *Turbulence and Chaotic Phenomena in Fluids*, edited by T. Tatsumi (Elsevier Science, New York, 1984), p. 39.
[32] M. Tadjfar and R. Bodonyi, Receptivity of a laminar boundary layer to the interaction of a three-dimensional roughness element with time-harmonic free-stream disturbances, J. Fluid Mech. **242**, 701 (1992).
[33] M. Choudhari, Boundary-layer receptivity due to distributed surface imperfections of a deterministic or random nature, Theor. Comput. Fluid Dyn. **4**, 101 (1993).
[34] J. Crouch, Localized receptivity of boundary layers, Phys. Fluids **4**, 1408 (1992).
[35] A. K. Yusim and I. Utama, An investigation into the drag increase on roughen surface due to marine fouling growth, IPTEK Technology and Science **28**, 73 (2017).
[36] M. Schultz, J. Bendick, E. Holm, and W. Hertel, Economic impact of biofouling on a naval surface ship, Biofouling **27**, 87 (2011).
[37] P. Klebanoff, Effect of free-stream turbulence on a laminar boundary layer, Bull. Am. Phys. Soc. **16**, 1323 (1971).
[38] J. Kendall, Experimental study of disturbances produced in a pre-transitional laminar boundary layer by weak freestream turbulence, in *18th Fluid Dynamics and Plasmadynamics and Lasers Conference* (AIAA, 1985), p. 1695.
[39] A. Boiko, K. Westin, B. Klingmann, V. Kozlov, and P. Alfredsson, Experiments in a boundary layer subjected to free stream turbulence. Part 2. The role of TS-waves in the transition process, J. Fluid Mech. **281**, 219 (1994).
[40] J. Mans, H. De Lange, and A. Van Steenhoven, Sinuous breakdown in a flat plate boundary layer exposed to free-stream turbulence, Phys. Fluids **19**, 088101 (2007).

[41] J. Mans, Ph.D. thesis, Streak development and breakdown during bypass transition, Technische Universiteit Eindhoven (2007).
[42] P. Schlatter, L. Brandt, H. De Lange, and D. S. Henningson, On streak breakdown in bypass transition, Phys. Fluids **20**, 101505 (2008).
[43] K. Westin, A. Boiko, B. Klingmann, V. Kozlov, and P. Alfredsson, Experiments in a boundary layer subjected to free stream turbulence. Part 1. Boundary layer structure and receptivity, J. Fluid Mech. **281**, 193 (1994).
[44] K. Westin, A. Bakchinov, V. Kozlov, and P. Alfredsson, Experiments on localized disturbances in a flat plate boundary layer. Part 1. The receptivity and evolution of a localized free stream disturbance, Eur. J. Mech. B Fluids **17**, 823 (1998).
[45] A. Bakchinov, K. Westin, V. Kozlov, and P. Alfredsson, Experiments on localized disturbances in a flat plate boundary layer. Part 2. Interaction between localized disturbances and ts-waves, Eur. J. Mech. B Fluids **17**, 847 (1998).
[46] G. Balamurugan and A. Mandal, Experiments on localized secondary instability in bypass boundary layer transition, J. Fluid Mech. **817**, 217 (2017).
[47] H. W. Emmons, The laminar-turbulent transition in a boundary layer—Part I, J. Aeronaut. Sci. **18**, 490 (1951).
[48] S. Dhawan and R. Narasimha, Some properties of boundary layer flow during the transition from laminar to turbulent motion, J. Fluid Mech. **3**, 418 (1958).
[49] M. Asai, M. Minagawa, and M. Nishioka, The instability and breakdown of a near-wall low-speed streak, J. Fluid Mech. **455**, 289 (2002).
[50] A. A. Draad, G. D. C. Kuiken, and F. T. M. Nieuwstadt, Laminar-turbulent transition in pipe flow for Newtonian and non-Newtonian fluids, J. Fluid Mech. **377**, 267 (1998).
[51] R. Hansen and R. Little, Early turbulence and drag reduction phenomena in larger pipes, Nature (London) **252**, 690 (1974).
[52] A. Ram and A. Tamir, Structural turbulence in polymer solutions, J. Appl. Polym. Sci. **8**, 2751 (1964).
[53] M. Ohara, Triggered laminar-to-turbulent transition in pipe flows of dilute polymer solutions, Ph.D. thesis, Massachusetts Institute of Technology, 1968.
[54] R. W. Paterson and F. Abernathy, Turbulent flow drag reduction and degradation with dilute polymer solutions, J. Fluid Mech. **43**, 689 (1970).
[55] W. Castro and W. Squire, The effect of polymer additives on transition in pipe flow, Appl. Sci. Res. **18**, 81 (1968).
[56] I. J. Wygnanski and F. Champagne, On transition in a pipe. Part 1. The origin of puffs and slugs and the flow in a turbulent slug, J. Fluid Mech. **59**, 281 (1973).
[57] C. W. H. van Doorne and J. Westerweel, Measurement of laminar, transitional and turbulent pipe flow using stereoscopic-PIV, Exp. Fluids **42**, 259 (2007).
[58] C. Van Doorne, B. Hof, R. Lindken, J. Westerweel, and U. Dierksheide, Time resolved stereoscopic PIV in pipe flow. Visualizing 3D flow structures, in *Proceedings of Fifth International Symposium on Particle Image Velocimetry, Busan, South Korea, September* (2003), pp. 22–24.
[59] P. Virk, E. Merrill, H. Mickley, and K. Smith, The critical wall shear stress for reduction of turbulent drag in pipe flow, in Modern Developments in the Mechanics of Continua, edited by S. Eskinazi (Academic Press, New York, 1966), p. 37.
[60] J. Hand and M. C. Williams, Effect of secondary polymer structure on the drag-reducing phenomenon, J. Appl. Polym. Sci. **13**, 2499 (1969).
[61] W. White and D. M. McEligot, Transition of mixtures of polymers in a dilute aqueous solution, J. Basic Eng. **92**, 411 (1970).
[62] M. Escudier, F. Presti, and S. Smith, Drag reduction in the turbulent pipe flow of polymers, J. Non-Newtonian Fluid Mech. **81**, 197 (1999).
[63] L. Xi and M. D. Graham, Intermittent dynamics of turbulence hibernation in Newtonian and viscoelastic minimal channel flows, J. Fluid Mech. **693**, 433 (2012).
[64] S.-N. Wang, A. Shekar, and M. D. Graham, Spatiotemporal dynamics of viscoelastic turbulence in transitional channel flow, J. Non-Newtonian Fluid Mech. **244**, 104 (2017).

[65] A. Kushwaha, J. S. Park, and M. D. Graham, Temporal and spatial intermittencies within channel flow turbulence near transition, Phys. Rev. Fluids **2**, 024603 (2017).
[66] R. D. Whalley, J. S. Park, A. Kushwaha, D. J. C. Dennis, M. D. Graham, and R. J. Poole, Low-drag events in transitional wall-bounded turbulence, Phys. Rev. Fluids **2**, 034602 (2017).
[67] S. Ryu, E. Davis, J. S. Park, H. Zhang, and J. Y. Yoo, Wall-shear-stress-based conditional sampling analysis of coherent structures in a turbulent boundary layer, J. Fluids Eng. **143**, 041301 (2021).
[68] L. Xi and M. D. Graham, Active and Hibernating Turbulence in Minimal Channel Flow of Newtonian and Polymeric Fluids, Phys. Rev. Lett. **104**, 218301 (2010).
[69] S. Tamano, M. D. Graham, and Y. Morinishi, Streamwise variation of turbulent dynamics in boundary layer flow of drag-reducing fluid, J. Fluid Mech. **686**, 352 (2011).
[70] P. Klebanoff, W. Cleveland, and K. Tidstrom, On the evolution of a turbulent boundary layer induced by a three-dimensional roughness element, J. Fluid Mech. **237**, 101 (1992).
[71] A. Perry, T. Lim, and E. Teh, A visual study of turbulent spots, J. Fluid Mech. **104**, 387 (1981).
[72] A. Smith and D. W. Clutter, The smallest height of roughness capable of affecting boundary-layer transition, J. Aerosp. Sci. **26**, 229 (1959).
[73] A. L. Braslow and E. C. Knox, Simplified method for determination of critical height of distributed roughness particles for boundary-layer transition at Mach numbers from 0 to 5, Technical Report, National Advisory Committee for Aeronautics, Vol. 4363 (1958).
[74] F. E. Bailey and R. Callard, Some properties of poly (ethylene oxide) 1 in aqueous solution, J. Appl. Polym. Sci. **1**, 56 (1959).
[75] J. Wu and M. Tulin, Drag reduction by ejecting additive solutions into pure-water boundary layer, J. Basic Eng. **94**, 749 (1972).
[76] C. D. Meinhart, S. T. Wereley, and J. G. Santiago, A PIV algorithm for estimating time-averaged velocity fields, J. Fluids Eng. **122**, 285 (2000).
[77] A. Sciacchitano, F. Scarano, and B. Wieneke, Multi-frame pyramid correlation for time-resolved PIV, Exp. Fluids **53**, 1087 (2012).
[78] M. Motozawa, T. Kurosawa, T. Otsuki, K. Iwamoto, H. Ando, T. Senda, and Y. Kawaguchi, PLIF measurement of turbulent diffusion in drag-reducing flow with dosed polymer solution from a wall, J. Thermal Sci. Tech. **7**, 272 (2012).
[79] E. Winkel, G. Oweis, S. Vanapalli, D. Dowling, M. Perlin, M. Solomon, and S. Ceccio, High-Reynolds-number turbulent boundary layer friction drag reduction from wall-injected polymer solutions, J. Fluid Mech. **621**, 259 (2009).
[80] Y. Hou, V. Somandepalli, and M. Mungal, Streamwise development of turbulent boundary-layer drag reduction with polymer injection, J. Fluid Mech. **597**, 31 (2008).
[81] J. Crimaldi, Planar laser induced fluorescence in aqueous flows, Exp. Fluids **44**, 851 (2008).
[82] F. M. White and I. Corfield, *Viscous Fluid flow*, Viscous fluid flow. Rest of the information is complete Vol. 3 (McGraw-Hill, New York, 2006).
[83] J. Sheng, E. Malkiel, and J. Katz, Using digital holographic microscopy for simultaneous measurements of 3D near wall velocity and wall shear stress in a turbulent boundary layer, Exp. Fluids **45**, 1023 (2008).
[84] C.-M. Ho and P. Huerre, Perturbed free shear layers, Annu. Rev. Fluid Mech. **16**, 365 (1984).
[85] J. W. Kurelek, S. Yarusevych, and M. Kotsonis, Vortex merging in a laminar separation bubble under natural and forced conditions, Phys. Rev. Fluids **4**, 063903 (2019).
[86] X. Wu, P. Moin, J. M. Wallace, J. Skarda, A. Lozano-Durán, and J.-P. Hickey, Transitional-turbulent spots and turbulent-turbulent spots in boundary layers, Proc. Natl. Acad. Sci. USA **114**, E5292 (2017).
[87] V. S. R. Somandepalli, Combined PIV and PLIF measurements in a polymer drag reduced turbulent boundary layer, Ph.D. thesis, Stanford University, 2006.
[88] T. A. Brungart, H. Petrie, W. Harbison, and C. Merkle, A fluorescence technique for measurement of slot injected fluid concentration profiles in a turbulent boundary layer, Exp. Fluids **11**, 9 (1991).
[89] Y. L. Xiong, C.-H. Bruneau, and H. Kellay, A numerical study of two dimensional flows past a bluff body for dilute polymer solutions, J. Non-Newtonian Fluid Mech. **196**, 8 (2013).
[90] J. Kim, Evolution of a vortical structure associated with the bursting event in a channel flow, in *Turbulent Shear Flows 5* (Springer, 1987), pp. 221–233.

[91] W. Schanderl and M. Manhart, Reliability of wall shear stress estimations of the flow around a wall-mounted cylinder, Comput. Fluids **128**, 16 (2016).
[92] D. Samanta, Y. Dubief, M. Holzner, C. Schäfer, A. N. Morozov, C. Wagner, and B. Hof, Elasto-inertial turbulence, Proc. Natl. Acad. Sci. USA **110**, 10557 (2013).
[93] Y. Dubief, V. E. Terrapon, and J. Soria, On the mechanism of elasto-inertial turbulence, Phys. Fluids **25**, 110817 (2013).
[94] M. S. Boutilier and S. Yarusevych, Parametric study of separation and transition characteristics over an airfoil at low Reynolds numbers, Exp. Fluids **52**, 1491 (2012).
[95] C.-S. Yih, Instability due to viscosity stratification, J. Fluid Mech. **27**, 337 (1967).
[96] A. Harang, O. Thual, P. Brancher, and T. Bonometti, Kelvin–Helmholtz instability in the presence of variable viscosity for mudflow resuspension in estuaries, Environ. Fluid Mech. **14**, 743 (2014).
[97] R. Jacobs and P. Durbin, Simulations of bypass transition, J. Fluid Mech. **428**, 185 (2001).
[98] C. Kuan and T. Wang, Investigation of the intermittent behavior of transitional boundary layer using a conditional averaging technique, Exp. Therm. Fluid Sci. **3**, 157 (1990).
[99] S. Tamano, M. Itoh, T. Inoue, K. Kato, and K. Yokota, Turbulence statistics and structures of drag-reducing turbulent boundary layer in homogeneous aqueous surfactant solutions, Phys. Fluids **21**, 045101 (2009).
[100] Y. Hou, V. S. Somandepalli, and M. Mungal, A technique to determine total shear stress and polymer stress profiles in drag reduced boundary layer flows, Exp. Fluids **40**, 589 (2006).
[101] H. Petrie and A. A. Fontaine, Comparison of turbulent boundary layer modifications with slot-injected and homogeneous drag-reducing polymer solutions, American Society of Mechanical Engineers, Fluids Engineering **237**, 205 (1996).